Chemical Engineering Journal 148 (2009) 248–253

Contents lists available at ScienceDirect

Chemical Engineering Journal

journal homepage: www.elsevier.com/locate/cej

Photocatalytic activity and hydroxyl radical formation of carbon-doped TiO_2 nanocrystalline: Effect of calcination temperature

Qi Xiao*, Linli Ouyang

School of Resources Processing and Bioengineering, Central South University, Changsha 410083, China

ARTICLE INFO

Article history:
Received 21 August 2007
Received in revised form 13 August 2008
Accepted 25 August 2008

Keywords:
Carbon-doped TiO_2 nanocrystalline
Hydroxyl radical
Photocatalytic activity

ABSTRACT

Carbon-doped TiO_2 nanocrystalline was prepared by sol–gel auto-combustion method and characterized by X-ray diffraction, X-ray photoelectron spectra (XPS), Brunauer–Emmett–Teller method (BET), UV–vis diffuse reflectance spectroscopy (DRS). The analysis of $^{\bullet}OH$ radical formation on the sample surface under visible light irradiation was performed by fluorescence technique with using terephthalic acid, which readily reacted with $^{\bullet}OH$ radical to produce highly fluorescent product, 2-hydroxyterephthalic acids. It was found that the order of photocatalytic activity per unit surface area was the same as that of the formation rate of $^{\bullet}OH$ radicals unit surface area, namely, the greater the formation rate of $^{\bullet}OH$ radicals unit surface area was, the higher photocatalytic activity unit surface area was achieved, indicating that the photocatalytic activity unit surface area was positive correlation to the formation rate of $^{\bullet}OH$ radicals unit surface area over the catalysts. In this study, the optimum calcination temperature was 600 °C, at which the highest formation rate of $^{\bullet}OH$ radicals per unit surface area was, and thereby the highest photocatalytic activity per unit surface area was achieved. In addition, it could be found that the order of photocatalytic activity correlated very well with the amount of visible light absorption, namely, the stronger the visible light absorption, the higher the photocatalytic activity.

1. Introduction

Photocatalytic degradation of various organic and inorganic pollutants using solar energy has been reported [1–3]. TiO_2 was the most widely used photocatalyst because of its good activity, chemical stability, commercial availability, and inexpensiveness. However, only a small UV fraction of solar light (3–5%) could be utilized because of the wide band gap of TiO_2. Therefore, it was urgent to develop a particular photocatalyst sensitive to sunlight [4]. Recently, doping TiO_2 with nonmetal elements such as nitrogen [5], carbon [6], sulfur [7], iodine [8] noticeably improved the photocatalytic activity of TiO_2 under visible light. Various synthetic routes have been studied for carbon-doped TiO_2 nanoparticles. Khan et al. [6] synthesized chemically modified TiO_2 by controlled combustion of Ti metal in a natural gas flame. Irie et al. [9] prepared carbon-doped anatase TiO_2 nanoparticles by oxidative annealing of TiC under O_2 flow at 873 K. Sakthivel and Kwasch [10] reported the wet process synthesis of carbon-doped n-TiO_2 by hydrolysis of $TiCl_4$ with tetrabutylammonium hydroxide ($C_{16}H_{36}NOH$) followed by calcinations of the precipitates. Especially, Nagaveni et al. [11,12] reported that the solar photocatalytic degradation rates with combustion-synthesized nano-TiO_2 was 20 times higher for remazol brill blue R (RBBR), 4 times higher for methylene blue (MB) and 1.6 times higher for orange G (OG), compared to Degussa P-25 TiO_2. Their discovery inspired us to further develop combustion synthesis method to prepare carbon-doped TiO_2.

In the present study, we focused on the synthesis of carbon-doped TiO_2 nanoparticles using sol–gel auto-combustion technique with a unique combination of the chemical sol–gel process and the combustion process [13]. In addition, the excess fuel could be used as carbon source for fuel/oxidizer >1 in the reaction system. Therefore, crystallization of TiO_2 as well as carbon doping could take place at the same time during the calcinations. The prepared carbon-doped TiO_2 nanoparticles were characterized by X-ray diffraction (XRD), X-ray photoelectron spectra (XPS), Brunauer–Emmett–Teller method (BET), UV–vis diffuse reflectance spectroscopy (DRS). The aim of this study was to investigate the effect of calcination temperature on both photocatalytic activity and $^{\bullet}OH$ radical's formation over carbon-doped TiO_2 samples under visible light irradiation and correlate the photocatalytic degradation of MB with $^{\bullet}OH$ radicals formed over carbon-doped TiO_2 samples.

* Corresponding author. Tel.: +86 731 8830543; fax: +86 731 8879815.
E-mail address: xiaoqi88@mail.csu.edu.cn (Q. Xiao).

1385-8947/$ – see front matter © 2008 Elsevier B.V. All rights reserved.
doi:10.1016/j.cej.2008.08.024

2. Experimental

2.1. Preparation of carbon-doped TiO_2 nanocrystalline

Carbon-doped TiO_2 nanocrystalline was synthesized by sol–gel auto-combustion technique. The detailed process can be described as follows. The analytical grade titanium isopropoxide ($Ti(OC_2H_5)_4$), $C_2H_6O_2$ (ethylene glycol, abbreviated as EG), $C_6H_8O_7$ (citric acid, abbreviated as CA), ammonia (25%) and nitride acid (65–68%) were used as raw materials. Appropriate amount of $Ti(OC_2H_5)_4$ was added to CA and EG mixture under constant stirring condition. The molar ratios of CA/Ti, NO_3^-/CA, and CA/EG were kept constant at 2:1, 1:3, and 1:1, respectively. After adjusting the pH value with ammonia to 6–7, the mixture solution was evaporated at 90 °C to gradually form a clear precursor gel. The precursor gel was baked at 150 °C in muffle furnace and expanded, then was auto-ignited at about 250 °C. The puffy, porous gray powders as-combusted was calcined at the temperature of 400–800 °C for 2 h in air, and quenched in air to room temperature.

2.2. Characterization of carbon-doped TiO_2 nanocrystalline

The crystalline structure of the samples was determined by a D/max-γA diffractometer (Cu Kα radiation, $\lambda = 0.154056$ nm) studies. The averaged grain sizes D were determined from the XRD pattern according to the Scherrer equation $D = k\lambda/\beta\cos\theta$, where k was a constant (shape factor, about 0.9), λ is the X-ray wavelength (0.15418 nm), β the full width at half maximum (FWHM) of the diffraction line, and θ the diffraction angle. The values of β and θ of anatase and rutile were taken from anatase (1 0 1) and rutile (1 1 0) diffraction line, respectively. The amount of rutile in the samples was calculated using the following equation [14]: $X_R = (1 + 0.8I_A/I_R)^{-1}$, where X_R was rutile weight percent, I_A and I_R were the integrated diffraction peak intensities from anatase (1 0 1) and rutile (1 1 0) peak intensity, respectively.

The specific surface area of the powders was measured by the dynamic BET method, in which a N_2 gas was adsorbed at 77 K using a Micromeritics ASAP 2000 system. To study the light absorption of the photocatalyst sample, DRS of the photocatalyst sample in the wavelength range of 200–800 nm were obtained using a UV–vis scanning spectrophotometer (Shimadzu UV-3101), while $BaSO_4$ was as a reference. XPS measurements were performed in a VG Scientific ESCALAB Mark II spectrometer equipped with two ultra-high vacuum (UHV) chambers using Al Kα radiation (1486.6 eV). The XPS binding energies were calibrated with respect to the C 1s peak from the carbon tape at 284.6 eV.

2.3. Determination of $^{\bullet}OH$ radicals

The analysis of $^{\bullet}OH$ radical's formation on the sample surface under visible light irradiation was performed by fluorescence technique with using terephthalic acid, which readily reacted with $^{\bullet}OH$ radicals to produce highly fluorescent product, 2-hydroxyterephthalic acid 15]. The intensity of the peak attributed to 2-hydroxyterephtalic acid was known to be proportional to the amount of $^{\bullet}OH$ radicals formed [15]. The selected concentration of terephthalic acid solution was 5×10^{-4} M in a diluted NaOH aqueous solution with a concentration of 2×10^{-3} M. It has been proved that at these experimental conditions (low concentration of terephthalic acid, less than 10^{-3} M, room temperature), the hydroxylation reaction of terephthalic acid proceeds mainly by $^{\bullet}OH$ radicals [15].

200 mg of the prepared carbon-doped TiO_2 samples was added to 200 mL of the 5×10^{-4} M terephthalic acid solution in 2×10^{-3} M NaOH, and then visible light irradiation of the solution was started. For visible light irradiation, a 150-W halogen tungsten lamp with a UV and IR cut-off filter acted as a visible light source to provide light emission at 400–800 nm. Sampling was performed in every 15 min. Solution after filtration through 0.45 μm membrane filter was analyzed on a Hitachi F-4500 fluorescence spectrophotometer. The product of terephthalic acid hydroxylation, 2-hydroxyterephthalic acid, gave a peak at the wavelength of about 425 nm by the excitation with the wavelength of 315 nm.

2.4. Photocatalytic activity

In order to evaluate photoactivity of the prepared samples, photocatalytic decomposition of MB was performed. For a typical photocatalytic experiment, 200 mg of the as-prepared carbon-doped TiO_2 nanocrystalline was added to 200 mL of the 100-ppm MB aqueous solution. The as-prepared carbon-doped TiO_2 samples were dispersed under ultrasonic vibration for 10 min. The suspension was kept in the dark under stirring to measure the adsorption of MB into each sample. After keeping at least 20 min, MB concentration in the solution was found to be constant on all samples. Therefore, the solution in which the sample powders were dispersed was kept in the dark for 30 min and then visible light irradiation of the solution was started. For visible light irradiation, a 150-W halogen tungsten lamp with a UV and IR cut-off filter acted as a visible light source to provide light emission at 400–800 nm. The lamp was positioned inside a cylindrical vessel and surrounded by a circulating water jacket to cool it. After recovering the catalyst by centrifugation, the light absorption of the clear solution was measured at 660 nm (λ_{max} for MB) at a set time. The absorbance of the MB solution was measured with a UV–vis spectrophotometer (Shimadzu UV-3101).

3. Results and discussion

3.1. XRD analysis

Fig. 1 showed the XRD patterns of TiO_2 powders calcined at various temperatures between 400 and 800 °C. It was shown that the sample was amorphous at calcination temperature of 400 °C. From these XRD results, it was shown that the X-ray diffraction peak at 25.5° corresponded to characteristic peak of crystal plane (1 0 1) of anatase, and the peak at 27.6° corresponded to characteristic peak of crystal plane (1 1 0) of rutile. The intensities of the anatase peaks decreased; while the intensities of the rutile peaks greatly increased and contents of

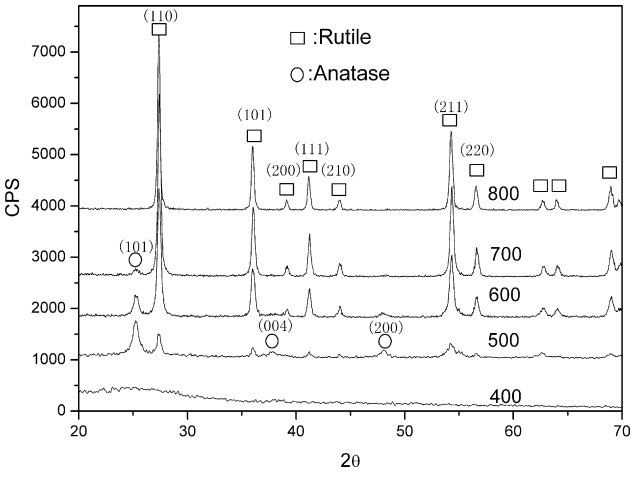

Fig. 1. XRD patterns of carbon-doped TiO_2 calcined at different calcination temperatures.

Table 1
The characteristics of carbon-doped TiO_2 prepared at various calcinations temperatures

Calcinations temperature(°C)	Anatase		Rutile		Specific surface area (m^2/g)	Decolourization of MB at 120 min (%)
	Crystal size, $D_{(101)}$ (nm)	X_A (%)	Crystal size, $D_{(110)}$ (nm)	X_R (%)		
500	13.5	54.76	16.00	45.24	20.00	49.16
600	–	10.76	17.73	89.24	18.8	52.58
700	–	0.41	23.64	97.59	16.65	43.48
800	–	0	24.22	100	15.50	39.16

rutile phase increased as the calcination temperature was raised (shown in Table 1). When calcined at 800 °C, the pattern exhibited a complete rutile TiO_2 structure, indicating that the phase transformation from anatase to rutile has completed at this temperature.

3.2. XPS studies

According to the XPS survey spectrum (Fig. 2A) of carbon-doped TiO_2 calcined at 600 °C for 2 h, the sample contained only Ti, O, and C. And binding energies for Ti $2p_{3/2}$, O 1s, and C 1s were 458.1, 529.9 and 288.2 eV, respectively.

To investigate the carbon states in the photocatalyst, we measured C 1s core levels, as shown in Fig. 2B. Deconvolution of the C 1s spectrum (Fig. 2B) revealed three components at 284.5, 288.0 and 290.3 eV. The smaller component at a binding energy of 284.5 eV could be attributed to C 1s electrons from the carbon tape. Sakthivel and Kwasch [10] observed the two kinds of carbonate species with binding energies of 287.5 and 288.5 eV. Ohno et al. [16] observed only one kind of carbonate species with binding energies of 288.0 eV, and they thought that C^{4+} ions were incorporated into the bulk phase of TiO_2. Li et al. [17] also observed only one kind of carbonate species with binding energies of 288.2 eV. Recently, Ren et al. [18] observed only one kind of carbonate species with binding energies of 288.6 eV and revealed that carbon may substitute for some of the lattice titanium atoms and form a Ti–O–C structure. These results indicated this main C 1s XPS peak (288.0 eV) could be assigned to Ti–O–C structure in carbon-doped titania by substituting some of the lattice titanium atoms by carbon in this work. In addition, the smaller component at a binding energy of 290.3 eV could be attributed to O=C–O components, which was similar to that of Tseng et al. [19].

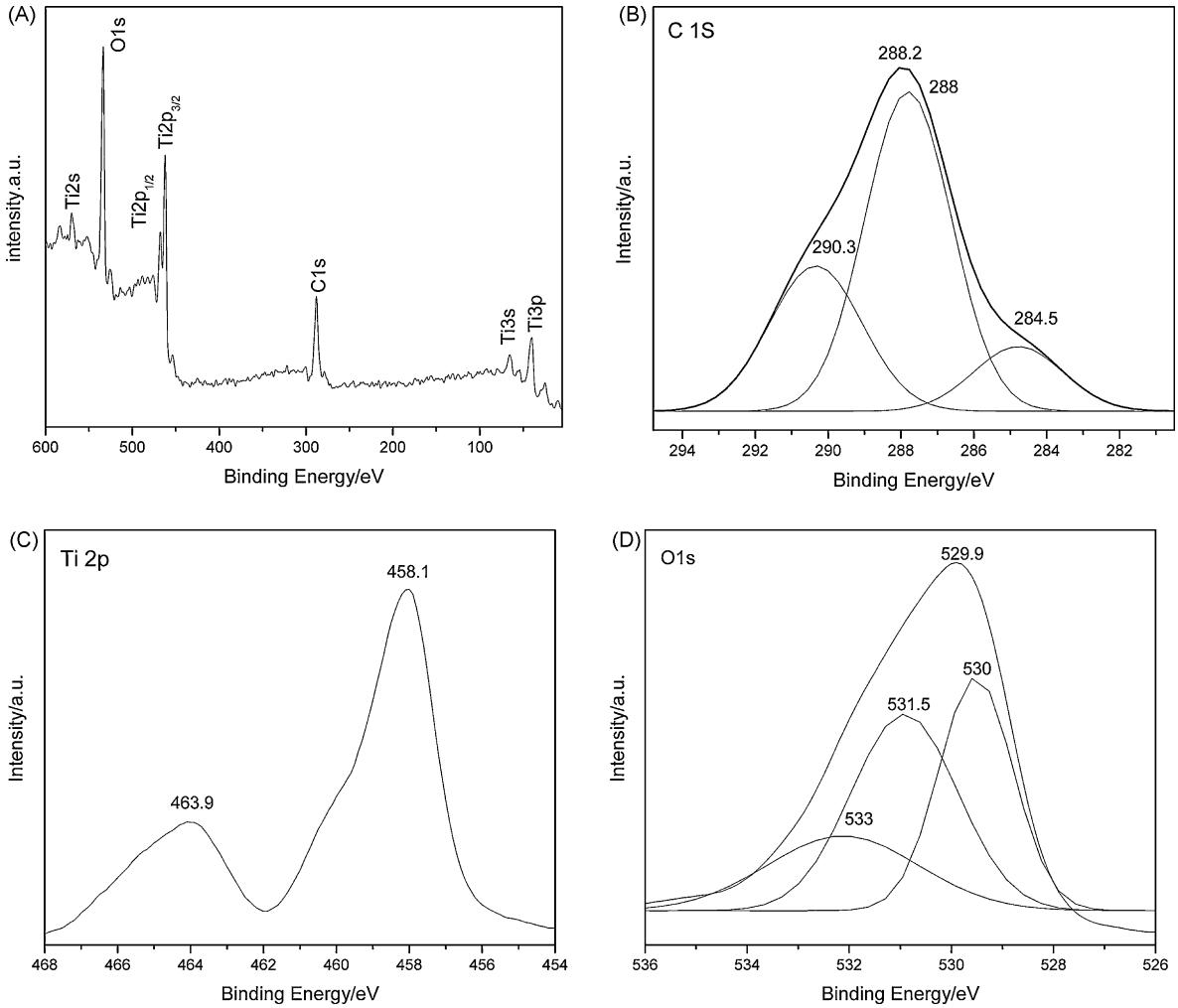

Fig. 2. XPS spectra of (A) survey spectrum, (B) C 1s, (C) Ti 2p, and (D) O 1s for carbon-doped TiO_2 calcined at 600 °C for 2 h.

XPS signals of Ti 2p were observed at binding energies at around 458.1 eV (Ti $2p_{3/2}$) and 463.9 eV (Ti $2p_{1/2}$), as shown in Fig. 2C. The typical binding energy of Ti $2p_{3/2}$ peak in TiO_2 crystals was 458.5–459.7 eV [20,21]. Typically, the binding energy of Ti $2p_{3/2}$ peak for P25 powder was 459.7 eV. Compared to the binding energy of Ti^{4+} in pure titania (458.5–459.7 eV), there was a red shift of binding energy of Ti $2p_{3/2}$ peak for the carbon-doped titania, which suggests that Ti^{3+} species was formed in the carbon-doped titania [16]. This result was in accordance with our preparation conditions, in which fuel/oxidizer > 1 implied fuel-rich condition, and Ti^{4+} species could be reduced into Ti^{3+} species.

Deconvolution of the O 1s spectrum was shown in Fig. 2D. The BE values of the individual components were 530.0 (Ti^{4+}–O) and 533 eV (OH^-), in agreement with previous work [22,23]. The BE components at 531.5 eV were unambiguously assigned to oxygen bonded to Ti^{3+} [24].

3.3. UV–vis spectra

Fig. 3 showed the UV–vis diffuse reflectance spectra of carbon-doped TiO_2 nanoparticles calcined at different calcinations temperatures. The absorption edge of the carbon-doped TiO_2 samples calcined at 400, 500, 600, 700, and 800 °C occurred at 418, 422, 433, 428, and 425 nm, respectively, and accordingly the band gap energy was estimated to be about 2.97, 2.94, 2.86, 2.90, and 2.92 eV, respectively. This showed that the band gap of the carbon-doped TiO_2 samples monotonically became narrower with the increase of calcinations temperatures, and the band gap of carbon-doped TiO_2 samples calcined at 873 K became the narrowest among all the carbon-doped TiO_2 samples. Herein, two reasons might account for high visible light activity of the as-synthesized carbon-doped TiO_2: (1) Ti–O–C structure in carbon-doped titania might be one of the reasons for the visible light photocatalytic activity, which was in accordance with previous results reported by Ren et al. [18]. (2) The presence of Ti^{3+} species produced in the process of carbon doping of the TiO_2 led to the formation of oxygen vacancy state in the as-synthesized carbon-doped TiO_2 between the valence and the conduction bands in the TiO_2 band structure. It was reported that reducing TiO_2 introduces localized oxygen vacancy states located at 0.75–1.18 eV below the conduction band edge of TiO_2 [25]. So, for TiO_2 containing localized oxygen vacancy, the band gap between valence band and localized oxygen vacancy state was 2.45–2.02 eV, which corresponded to a wavelength of 506–614 nm. Our DRS showed that the carbon-doped TiO_2 had an obvious absorption up to 600 nm (mainly in the region of 450–600 nm) as shown in Fig. 3. Therefore, the formation of Ti^{3+} species in the as-synthesized carbon-doped TiO_2 was another reason for the visible light photocatalytic activity.

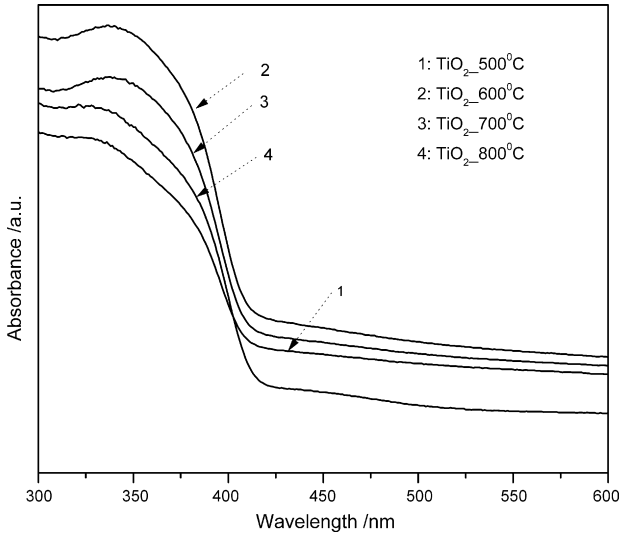

Fig. 3. UV–vis absorption spectra of carbon-doped TiO_2 calcined at different calcination temperatures.

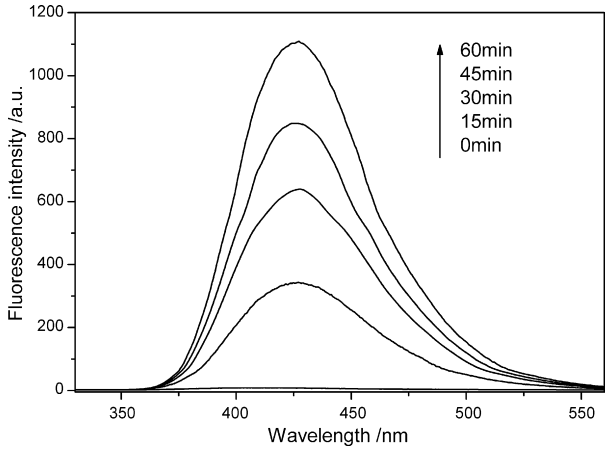

Fig. 4. Fluorescence spectral changes observed during illumination of carbon-doped TiO_2 calcined at 600 °C for 2 h in 4×10^{-4} M NaOH solution of terephthalic acid (excitation at 315 nm). Each fluorescence spectrum was recorded every 15 min of UV illumination.

3.4. Formation of $^{\bullet}OH$ radicals

The fluorescence emission spectrum (excitation at 315 nm) of terephthalic acid solution was measured every 15 min during illumination. Fig. 4 showed the induction of fluorescence from 5×10^{-4} M terephthalic acid solution in 2×10^{-3} M NaOH. As shown in the figures, gradual increase in the fluorescence intensity at about 425 nm was observed with increasing illumination time. Based on the reports in radiation chemistry [26] and sonochemistry [27–29], it was reasonable to assume that photogenerated O_2^-, $HO_2^{\bullet}$ and H_2O_2 did not interfere with the reaction between $^{\bullet}OH$ and terephthalic acid. Moreover, the generated spectrum had the identical shape and maximum wavelength with that of 2-hydroxyterephthalic acid. These results suggested that fluorescent products formed during carbon-doped TiO_2 were due to the specific reaction between $^{\bullet}OH$ radicals and terephthalic acid.

Fig. 5 showed the plots of increase in fluorescence intensity against illumination time at 425 nm. The fluorescence intensity by visible light illumination in terephthalic acid solutions increased almost linearly against time. Consequently, we could conclude that $^{\bullet}OH$ radicals formed at the carbon-doped TiO_2 interface were in proportional to the light illumination time obeying zero-order reaction rate kinetics. The formation rate of $^{\bullet}OH$ radicals could be expressed by the slop of these lines shown in Fig. 5. In Fig. 6, the formation rate of $^{\bullet}OH$ radical's k_{OH} was plotted against calcination temperature. The formation rate of $^{\bullet}OH$ radicals k_{OH} increased with increasing the calcination temperatures and gave a maximum at 600 °C, then decreased with increasing calcination temperatures above 600 °C. It could be related to the absorption spectra presented in Fig. 3, because carbon-doped TiO_2 calcined at 600 °C showed stronger absorption not only in the 400–500 nm but also in the 300–400 nm range compared to the other carbon-doped TiO_2 samples.

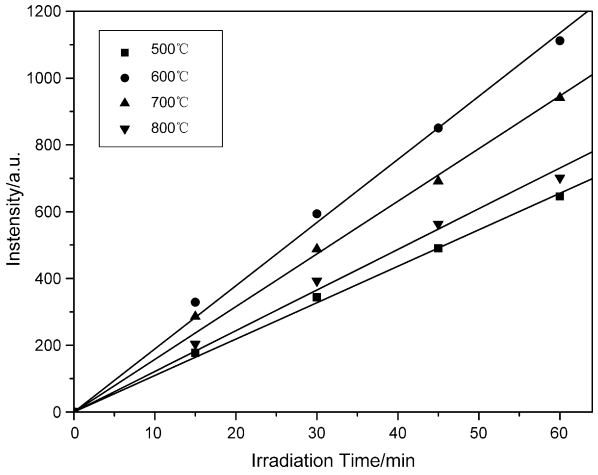

Fig. 5. Plots of the induced fluorescence intensity at 426 nm against irradiation time for terephthalic acid on carbon-doped TiO_2 calcined at different calcination temperatures.

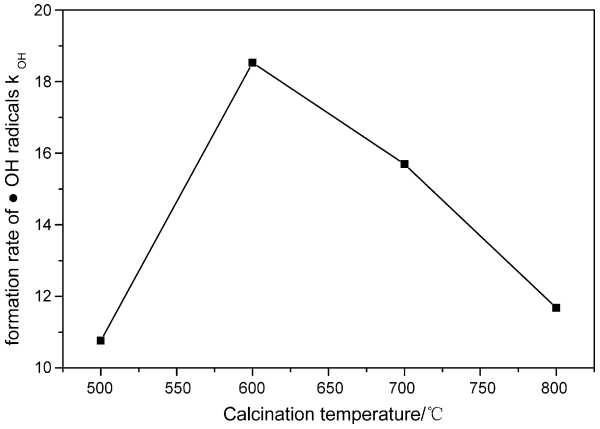

Fig. 6. The effect of calcination temperatures on formation rate of $^{\bullet}$OH radical's k_{OH}.

3.5. Photocatalytic activity of carbon-doped TiO_2

Fig. 7 showed the results of photocatalytic decomposition of MB over carbon-doped TiO_2 prepared at various calcination temperatures. It was found that the photocatalytic activity increased up to the sample calcined at 600 °C for 2 h with increasing calcination temperatures, and the photocatalytic activity decreased with increasing calcination temperatures above 600 °C, which indicated that the optimum calcination temperature was 600 °C.

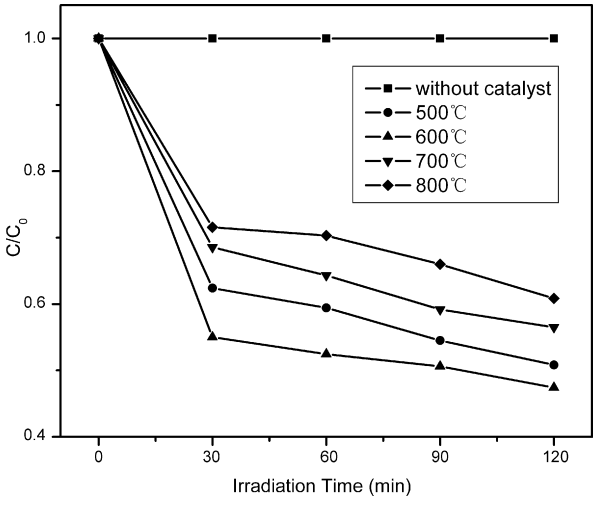

Fig. 7. Photocatalytic decomposition profiles of methylene blue over carbon-doped TiO_2 nanocrystalline calcined at different calcination temperatures.

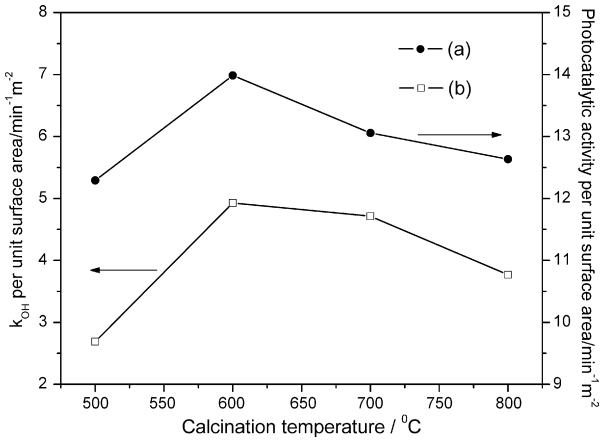

Fig. 8. The effect of calcinations temperatures on (a) the photocatalytic activity per unit surface area and (b) formation rate of $^{\bullet}$OH radicals k_{OH} per unit surface area.

According to Figs. 6 and 7, it was found that both there existed a optimum calcination temperature 600 °C for the photocatalytic activity and formation rate of $^{\bullet}$OH radicals k_{OH}. However, according to the BET analysis (shown in Table 1), the increase of calcination temperature reduced the surface area that was 20, 18.8, 16.65, and 15.50 m^2/g at 500, 600, 700, and 800 °C, respectively. The reduction of surface area would lead to the decrease of active sites on which the reactants could adsorb. So, the increase of calcination temperature seemed to be not helpful for the photocatalytic activity and formation rate of $^{\bullet}$OH radical's k_{OH}. In order to remove the influence of the surface-area reduction on the photocatalytic activity and formation rate of $^{\bullet}$OH radicals $k_{OH,}$ both the photocatalytic activity per unit surface area and formation rate of $^{\bullet}$OH radicals k_{OH} per unit surface area were used in Fig. 8. It was found that the order of photocatalytic activity per unit surface area was the same as that of the formation rate of $^{\bullet}$OH radicals unit surface area, namely, the greater the formation rate of $^{\bullet}$OH radicals unit surface area was, the higher photocatalytic activity unit surface area was achieved, indicating that the photocatalytic activity unit surface area was positive correlation to the formation rate of $^{\bullet}$OH radicals unit surface area over the catalysts. During the photocatalytic process, the absorption of photons by the photocatalysts led to the excitation of electrons from the valence band to the conduction band, thus generating electron-hole pairs. Oxygen molecules dissolved in the suspension captured the electron in the conduction band, and the hole in the valence band was captured by H_2O species adsorbed on the surface of the catalysts, to produce the $^{\bullet}$OH radicals, which subsequently oxidized an adsorbed pollutants. According to Ammar et al. [30], firstly the $^{\bullet}$OH radical generated through the oxidation of water molecules adsorbed on TiO_2, and then $^{\bullet}$OH radical oxidized the adsorbed MB molecules. For that reason, the greater the formation rate of $^{\bullet}$OH radicals was, the higher photocatalytic activity was achieved.

4. Conclusion

It was found that the order of photocatalytic activity per unit surface area was the same as that of the formation rate of $^{\bullet}$OH radicals unit surface area, namely, the greater the formation rate of $^{\bullet}$OH radicals unit surface area was, the higher photocatalytic activity unit surface area was achieved, indicating that the pho-

tocatalytic activity unit surface area was positive correlation to the formation rate of $^{\bullet}$OH radicals unit surface area over the catalysts. In this study, the optimum calcination temperature was 600 °C, at which the highest formation rate of $^{\bullet}$OH radicals per unit surface area was, and thereby the highest photocatalytic activity per unit surface area was achieved. In addition, it could be found that the order of photocatalytic activity correlated very well with the amount of visible light absorption, namely, the stronger the visible light absorption, the higher the photocatalytic activity.

Acknowledgements

This work was supported by the Provincial Excellent PhD Thesis Research Program of Hunan (No. 2004-141) and the Postgraduate Educational Innovation Fund of Central South University (No. 2006-48).

References

[1] B. Neppolian, H.C. Choi, S. Sakthivel, B. Arabindoo, V. Murugesan, Chemosphere 46 (2002) 1173.
[2] S. Sakthivel, B. Neppolian, M.V. Shankar, B. Arabindoo, M. Palanichamy, V. Murugesan, Sol. Energy Mater. Sol. Cells 77 (2003) 65.
[3] W.S. Kuo, P.H. Ho, Chemosphere 45 (2001) 77.
[4] J. Tang, Z. Zou, J. Ye, Chem. Mater. 16 (2004) 1644.
[5] R. Asashi, T. Morikawa, T. Ohwaki, K. Aoki, Y. Taga, Science 293 (2001) 269.
[6] S.U.M. Khan, M. Al-shahry, W.B. Ingler Jr., Science 297 (2002) 2243.
[7] T. Umebayashi, T. Yamaki, H. Itoh, K. Asai, Appl. Phys. Lett. 81 (2002) 454.
[8] X.T. Hong, Z.P. Wang, W.M. Cai, F. Lu, J. Zhang, Y.Z. Yang, N. Ma, Y.J. Liu, Chem. Mater. 17 (2005) 1548.
[9] H. Irie, Y. Watanabe, K. Hashimoto, Chem. Lett. 32 (2003) 772.
[10] S. Sakthivel, H. Kwasch, Angew. Chem. Int. Ed. 42 (2003) 4908.
[11] K. Nagaveni, G. Sivalingam, M.S. Hegde, G. Madras, Appl. Catal. B: Environ. 48 (2004) 83.
[12] K. Nagaveni, M.S. Hegde, N. RaVishankar, G.N. Subbanna, G. Madras, Langmuir 20 (2004) 2900.
[13] R.K. Selvan, C.O. Augustin, L.J. Berchmans, R. Saraswathi, Mater. Res. Bull. 38 (2003) 41.
[14] R.A. Spurr, H. Myers, Anal. Chem. 29 (1957) 760.
[15] K. Ishibashi, A. Fujishima, T. Watanabe, K. Hashimoto, Electrochem. Commun. 2 (2000) 207.
[16] T. Ohno, T. Tsubota, M. Toyofuku, R. Inaba, Catal. Lett. 98 (2004) 255.
[17] Y. Li, D.-S. Hwang, N.H. Lee, S.-J. Kim, Chem. Phys. Lett. 404 (2005) 25.
[18] W. Ren, Z. Ai, F. Jia, L. Zhang, X. Fan, Z. Zou, Appl. Catal. B: Environ. 69 (2007) 138.
[19] Y.-H. Tseng, C.-S. Kuo, C.-H. Huang, Y.-Y. Li, P.-W. Li, C.-L. Cheng, M.-S. Wong, Nanotechnology 17 (2006) 2490.
[20] M. Yoshitake, A. Thananan, T. Aizawaki, K. Yoshihara, Surf. Interface Anal. 34 (2002) 698.
[21] Y.L. Wang, Surf. Coat. Technol. 150 (2002) 257.
[22] A.F. Carley, G. Spoto, P.R. Chalker, J.C. Riviere, M.W. Roberts, J. Chem. Soc., Faraday Trans. I 83 (1987) 351.
[23] J. Pouilleau, D. Devilliers, H. Groult, P. Marcus, J. Mater. Sci. 32 (1998) 5645.
[24] P. Madhu Kumar, S. Badrinarayanan, M. Sastry, Thin Solid Films 358 (2000) 122.
[25] N. Isao, N. Nobuaki, K. Shuzo, I. Tatsuhiko, S. Shinichi, T. Koji, J. Mol. Catal. A: Chem. 161 (2000) 205.
[26] H.M. Khan, M. Anwar, G. Ahmad, J. Radioanal. Nucl. Chem. Lett. 200 (1995) 521.
[27] T.J. Mason, J.P. Lorimer, D.M. Bates, Y. Zhao, Ultrasonics Sonochem. 1 (1994) S91.
[28] X. Fang, M. Gertraud, C. von Sonntag, Ultrasonics Sonochem. 3 (1996) 57.
[29] J.C. Barreto, G.S. Smith, N.H.P. Strobel, P.A. McQuillin, T.A. Miller, Life Sci. 56 (1994) L89.
[30] H. Ammar, L. Hinda, K. Mohamed, E. Elimame, G. Chantal, H. Jean-Marie, Appl. Catal. B: Environ. 31 (2001) 145.